Submitted to the International Europhysics Conference on High Energy Physics,
HEP97, Jerusalem, Israel, August 1997

Measurement of the Inclusive Di-Jet Cross Section in Photoproduction and Determination of an Effective Parton Distribution in the Photon

H1 Collaboration

Abstract

The double-differential inclusive di-jet cross section in photoproduction processes is measured with the H1 detector at HERA. The cross section is determined as a function of the average transverse jet energy $E_T^{\rm jets}$ for ranges of the fractional energy $x_\gamma^{\rm jets}$ of the parton from the photon side. An effective leading order parton distribution in the photon is determined at large parton fractional energies for scales between $80 < p_T^2 < 1250\,{\rm GeV}^2$. The measurement is compatible with the logarithmic scale dependence that is predicted by perturbative QCD.

Abstract 268
Parallel Sessions 2, 3, 4
Plenary Sessions 1, 2, 3

1 Introduction

In lepton–proton collisions at HERA the cross section is dominated by processes in which the lepton radiates a quasi-real photon which then interacts with the proton. In a small fraction of such events, jets are formed [1, 2, 3, 4, 5]. In the leading-order interpretation of QCD, the jets result either from *direct* photon interactions with the partons of the proton (Fig. 1a) or from *resolved* photon–proton processes (Fig. 1b), where the photon interacts with the partons of the proton via its own parton content. For resolved photon processes, parton densities of the photon $f_{i/\gamma}(x_\gamma, \mu^2)$ are defined which give the probability of finding a parton i in the photon carrying a fraction x_γ of the photon's energy. The scale, μ, at which the photon is probed in the parton–parton collision is here considered to be the transverse momentum p_T of the scattered partons.

In this paper, a measurement of the inclusive di-jet cross section $\mathrm{d}^2\sigma/(\mathrm{d}x_\gamma^{\mathrm{jets}}\mathrm{d}\log(E_T^{\mathrm{jets}})^2)$ is presented as a function of the observed parton fractional energy $0.1 < x_\gamma^{\mathrm{jets}} < 1$ and of the squared average jet transverse energy $100 < (E_T^{\mathrm{jets}})^2 < 2500\,\mathrm{GeV}^2$. Throughout the paper we denote observed hadronic variables that were corrected for detector effects with the suffix 'jet', reconstructed quantities from the detector with the suffix 'rec', and leave variables referring to the partons without an additional suffix. All transverse energies are determined with respect to the ep beam axis.

The measurement is compared with QCD calculations of the cross section which require parton distributions of the proton and the photon as input. In the kinematic range relevant to this analysis, the parton distributions of the proton are well measured. The largest uncertainty in the results of the calculations comes from the quark and gluon densities of the photon. The quark density functions used in the calculations were determined from measurements of the photon structure function F_2^γ in deep inelastic electron–photon scattering at e^+e^- colliders. These experiments covered the kinematic range $0.05 < x_\gamma < 0.9$ and $\mu^2 = Q^2 < 400\,\mathrm{GeV}^2$ where Q^2 is the virtuality of the photon which probes the quasi-real photon (PETRA [6, 7, 8, 10, 11], PEP [9], TRISTAN [12, 13] and LEP [14, 15]). In contrast to these F_2^γ measurements, the photoproduction of jets is sensitive to both the quark and gluon content of the photon already in leading order. A first measurement of the gluon distribution in the photon has been made in the range $0.04 < x_\gamma < 1$ at the scale $p_T^2 = 75\,\mathrm{GeV}^2$ [2]. The comparison of the measured di-jet cross section with the QCD calculations provides both a test of the universality of the parton densities in the photon and gives new information on the parton densities.

In addition to predicting the parton–parton scattering processes between the photon and the proton, perturbative QCD predicts characteristic features of the quark density $f_{\mathrm{q}/\gamma}$ in the photon [16]. The general characteristics are given by the DGLAP evolution equation for the photon

$$\frac{\mathrm{d}f_{\mathrm{q}/\gamma}(x_\gamma,\mu)}{\mathrm{d}\ln(\mu^2/\Lambda^2_{\mathrm{QCD}})} = a\,\alpha\,P_{\mathrm{q}\gamma}(x_\gamma) + b\,\alpha_s \int_{x_\gamma}^1 \frac{\mathrm{d}z}{z}\left[P_{\mathrm{qq}}\left(\frac{x_\gamma}{z}\right) f_{\mathrm{q}/\gamma}(z,\mu) + P_{\mathrm{qg}}\left(\frac{x_\gamma}{z}\right) f_{\mathrm{g}/\gamma}(z,\mu)\right] \quad (1)$$

where a and b are constant, α and α_s are the fine structure constant and the strong coupling constant respectively, Λ_{QCD} is the QCD scale parameter, and P_{ij} are the splitting functions. While the form of the integral on the right hand side is the same as that for hadrons, the inhomogeneous term $a\,\alpha\,P_{\mathrm{q}\gamma}$ is peculiar to the photon: it reflects the contribution of quarks from the pointlike coupling of the photon to a quark–anti-quark pair. Solving (1), the asymptotic behaviour of $f_{\mathrm{q}/\gamma}$ at large scale μ and medium x_γ is predicted to be [16]

$$f_{\mathrm{q}/\gamma} \sim \ln\frac{\mu^2}{\Lambda^2_{\mathrm{QCD}}}\ . \quad (2)$$

The increase of the parton density with increasing scale is clearly different from the behaviour of the parton density distributions of hadrons and is referred to as the anomalous hadronic structure of the photon.

In this analysis, the QCD prediction for the scale dependence of the quark densities in the photon is tested using the di-jet measurements. Since in the photoproduction of jets the incoming quarks and gluons cannot be distinguished, an effective parton density $\tilde{f}_\gamma$ of the photon is extracted from the data. This contains a combination of the quark and gluon densities and is valid in leading-order QCD [17]. The measured effective parton density is compared with different predictions.

2 Detector Description

A detailed description of the H1 detector can be found elsewhere [18]. Here we describe only those components which are used in the analysis. The H1 central tracking system is mounted concentrically around the beam-line and covers polar angles between $20° < \theta < 160°$. The angle θ is measured with respect to the proton beam direction. The plane perpendicular to the z axis is termed $r - \phi$ plane. Measurements of the charge and momenta of charged particles are provided by two coaxial cylindrical drift chambers (central jet chambers, CJC) [19]. At two radial positions are placed a drift chamber, which provides accurate measurement of the z coordinate of charged tracks, and a multiwire proportional chamber (MWPC), which allows triggering on those tracks. These are located within the inner CJC and between the two jet chambers. The central tracking system is complemented by a forward tracking system which covers polar angles $7° \lesssim \theta \lesssim 25°$. In the present analysis the tracking detectors are used to define the vertex position along the beam axis and to support the measurement of the hadronic energy flow.

The tracking system is surrounded by a highly segmented liquid argon (LAr) sampling calorimeter [20] with an inner electromagnetic section consisting of lead absorber plates with a total depth of 20 to 30 radiation lengths and an outer hadronic section with steel absorber plates. The LAr calorimeter covers polar angles between 4° and 153° and its total depth is 4.5 to 8 interaction lengths, depending on the polar angle. The region $151° \lesssim \theta \lesssim 176°$ is covered by a lead scintillator calorimeter (BEMC).

A magnetic field of 1.15 T is produced by a superconducting solenoid surrounding the LAr calorimeter. The iron flux return yoke surrounding the superconducting solenoid is instrumented with limited streamer tubes to provide muon identification and measurement of energy leaking from the LAr and BEMC calorimeters.

All calorimeters provide measurement of the hadronic energy flow. Here, jet measurements are restricted to the range which is covered by the LAr calorimeter.

The luminosity is measured using the radiative process $ep \to ep\gamma$ where the photon is detected in a luminosity monitor.

3 Data Selection

The data were taken in 1994 with the H1 detector operating at the lepton–proton collider HERA, where positrons of 27.5 GeV collide with protons of 820 GeV. The integrated luminosity used for this analysis is $2.9\,\mathrm{pb}^{-1}$.

The photoproduction events were selected by requiring that the scattered electron remains in the beam pipe, undetected in the central H1 detector (so-called untagged events). The photon virtuality is therefore restricted to $Q^2 < 4\,\mathrm{GeV}^2$, where 80% of the events have $Q^2 < 0.1\,\mathrm{GeV}^2$.

The main trigger for untagged jet events is a summed transverse energy in the LAr calorimeter of at least 6 GeV with the additional requirement of a single energetic cluster of at least 2 GeV which is validated by a local coincidence of a track originating from the interaction vertex. Together with triggers that are purely based on the tracking detectors the untagged jet events are triggered with at least 80% efficiency over the whole kinematic range.

The fraction of the lepton beam energy E_e that is carried by the photon is denoted by $y = E_\gamma/E_\mathrm{e}$. It was approximately determined as y^rec from all reconstructed objects in the central detector, i.e. calorimeter clusters supported by tracking information, with transverse energy $E_{T,\mathrm{h}}^\mathrm{rec}$ and pseudo-rapidity $\eta_\mathrm{h}^\mathrm{rec} = -\ln(\tan\theta/2)$ using

$$y^\mathrm{rec} = \frac{1}{2E_\mathrm{e}} \sum_\mathrm{h} E_{T,\mathrm{h}}^\mathrm{rec} e^{-\eta_\mathrm{h}^\mathrm{rec}} \; . \tag{3}$$

The reconstructed scaled energy was restricted to the range $0.2 < y^\mathrm{rec} < 0.8$. The lower cut suppresses the contribution from background events that do not result from ep interactions. The remaining background is at the level of 1%. The upper cut reduces events from deep inelastic scattering at $Q^2 > 4\,\mathrm{GeV}^2$, where the scattered electron remained unidentified, to less than 1% of the total sample.

The jets were found using a cone algorithm [21] with cone size $R = 0.7$ and jet pseudo-rapidities in the range $-0.5 < \eta^\mathrm{rec} < 2.5$ in the HERA laboratory system. In this implementation of the cone algorithm, the jet cone position was chosen such that the transverse energy of the jet was maximal. The jet with the highest transverse energy was constructed first, the jet finding was then continued using only the remaining energy flow outside of the first jet cone. In case of overlapping jet cones, all energy flow in the overlap region was assigned to the jet with the higher transverse energy.

After these selection cuts, the total number of events with at least two jets reconstructed with a transverse energy above 7 GeV was 6499.

4 QCD Calculation of the Di-Jet Cross Section

In leading-order QCD the differential ep cross section for di-parton production can be written as follows:

$$\frac{\mathrm{d}^4\sigma}{\mathrm{d}y\,\mathrm{d}x_\gamma\,\mathrm{d}x_\mathrm{p}\,\mathrm{d}\cos\theta^*} = \frac{1}{32\pi s_\mathrm{ep}} \frac{f_{\gamma/\mathrm{e}}(y)}{y} \sum_{ij} \frac{f_{i/\gamma}(x_\gamma, p_T^2)}{x_\gamma} \frac{f_{j/\mathrm{p}}(x_\mathrm{p}, p_T^2)}{x_\mathrm{p}} |M_{ij}(\cos\theta^*)|^2 \; . \tag{4}$$

In this expression, s_ep denotes the squared lepton–proton center-of-mass energy available at HERA, $\sqrt{s_\mathrm{ep}} = 300\,\mathrm{GeV}$. The flux of photons radiated off the electron with fractional energy y is predicted by QED and is denoted by $f_{\gamma/\mathrm{e}}$. The fractional energy of the parton in the photon is given by x_γ and the parton density function of parton i in the photon by $f_{i/\gamma}$. The corresponding variables for the proton are x_p and $f_{j/\mathrm{p}}$. Note that, in contrast to the quark distribution in the photon mentioned in (1), $f_{i/\gamma}$ here represents all components in the photon including the direct photon processes and the quarks and gluons for resolved photon processes. The last term in (4) contains the distribution of the parton scattering angle θ^* in the parton–parton center-of-mass system in the form of the QCD matrix elements $M_{ij}(\cos\theta^*)$.

The parton transverse momentum p_T, which is here identified with the scale of the process, can be expressed in terms of the four observables in (4):

$$p_T^2 = \frac{1}{4} s_{\mathrm{ep}}\, y\, x_\gamma\, x_{\mathrm{p}}\, \sin^2\theta^* \ . \qquad (5)$$

For the correction of the data, and for comparison to the measured jet cross sections, the two event generators PYTHIA [22] and PHOJET [26, 27] were used. In both generators jet production is based on the leading-order di-parton cross section as given in (4).

The PYTHIA 5.7 event generator [22] was used to simulate photon-proton interactions. As well as the leading-order cross section (4), PYTHIA includes initial- and final-state parton radiation effects which are calculated in the leading logarithmic approximation. The strong coupling constant α_s is calculated in first order QCD using $\Lambda_{\mathrm{QCD}} = 200\,\mathrm{MeV}$ for 4 quark flavours. Multiple parton interactions were generated in addition to the primary parton–parton scattering. They are calculated as leading-order QCD processes between partons from the photon and proton remnants. The transverse momentum of all parton–parton interactions was required to be above $p_T = 1.2\,\mathrm{GeV}$. This cut-off value has been found to give an optimal description of the transverse energy flow outside the jets [3]. A good description of this energy flow is important since the contributions of multiple parton interactions inside the jet cones alter the jet rates considerably. For tests of the uncertainties in the determination of the effective parton distribution of the photon arising from the contribution of multiple parton interactions, an event sample was generated with $p_T > 1.4\,\mathrm{GeV}$, which gives an energy flow that is significantly smaller than that observed in the data. To assess the significance of higher-order effects, another sample was generated without initial-state parton showers. GRV-LO parameterizations were used throughout for the parton distributions of the photon and the proton [23, 24] and hadronization was modelled with the LUND string fragmentation scheme (JETSET 7.4 [25]).

The PHOJET 1.06 event generator [26, 27] is based on the two-component Dual Parton Model [28]. It calculates parton–parton scattering using (4). Again, Λ_{QCD} is $200\,\mathrm{MeV}$ for 4 quark flavours. PHOJET incorporates very detailed simulations of both multiple soft and hard parton interactions on the basis of a unitarization scheme [29]. It includes initial- and final-state hard parton radiation effects. The lower momentum cut-off for hard parton interactions was set to $p_T = 2.5\,\mathrm{GeV}$. In contrast to the PYTHIA generator, small variations of this cut-off value do not have a large influence on the results obtained by PHOJET, due to the unitarization scheme. For the fragmentation the LUND string concept is applied (JETSET 7.4 [25]). The GRV-LO parton distribution functions for the photon and the proton were also used here. The effects of higher-order corrections were checked by generating a sample of events without hard initial-state parton showers.

For comparisons with the measured jet cross sections, analytic QCD calculations were provided by ref. [30]. These calculations include the next-to-leading order (NLO) QCD matrix elements. They use the NLO parton distribution functions GRV-HO [23] and GS96 [31] for the photon and the CTEQ-4M distributions [32] for the partons of the proton.

5 Measurement of the Di-Jet Cross Section

In order to study observables closely related to the parton distributions in the photon, the differential di-jet cross sections were analysed in terms of the variables E_T^{jets} and x_γ^{jets}. The observable E_T^{jets} was calculated using the two jets with the highest E_T^{jet} in the event

$$E_T^{\mathrm{jets}} = \frac{E_T^{\mathrm{jet1}} + E_T^{\mathrm{jet2}}}{2} \qquad (6)$$

and was required to be above $E_T^{\rm jets} = 10\,{\rm GeV}$.

The ratio of the difference and the sum of the transverse energies of the jets was required to be in the range

$$\frac{|E_T^{\rm jet1} - E_T^{\rm jet2}|}{E_T^{\rm jet1} + E_T^{\rm jet2}} < 0.25\ . \tag{7}$$

The cuts (6) and (7) ensure that the transverse energy of all jets is above $E_T^{\rm jet} = 7.5\,{\rm GeV}$, without using the same $E_T^{\rm jet}$ cut-off for both jets. In next-to-leading order analytical calculations of the di-jet cross section this avoids introducing a dependence of the result on unphysical parameters.

The observable $x_\gamma^{\rm jets}$ was calculated using the transverse energies and pseudo-rapidities of the two jets and the photon energy:

$$x_\gamma^{\rm jets} = \frac{E_T^{\rm jet1} e^{-\eta^{\rm jet1}} + E_T^{\rm jet2} e^{-\eta^{\rm jet2}}}{2yE_{\rm e}}\ . \tag{8}$$

Here, the interval $0.1 < x_\gamma^{\rm jets} < 1$ is considered.

The average rapidity of the two jets was required to be in the range

$$0 < \frac{\eta^{\rm jet1} + \eta^{\rm jet2}}{2} < 2\ . \tag{9}$$

This variable is approximately the rapidity of the parton–parton center-of-mass system in the laboratory frame of reference. The difference in the jet pseudo-rapidities was required to be within

$$|\Delta\eta^{\rm jets}| < 1 \tag{10}$$

which corresponds to $|\cos\theta^{*,\rm jets}| < 0.46$. Together with (9) this cut ensures that all jets are in a region in which the hadronic energy is well measured in the detector.

In Fig. 2 the ep double-differential di-jet cross section is shown as a function of the transverse energy $E_T^{\rm jets}$ in bins of the fractional parton energy $x_\gamma^{\rm jets}$. The event kinematics corresponds to corrected photon fractional energies in the range

$$0.2 < y < 0.83 \tag{11}$$

and photon virtualities of

$$Q^2 < 4\,{\rm GeV}^2\ . \tag{12}$$

The di-jet cross section was corrected for detector effects using an unfolding procedure [33]. The procedure requires a 4-dimensional correlation function between the variables reconstructed in the detector $(x_\gamma^{\rm rec}, E_T^{\rm rec})$ and the corrected observables referring to the hadronic final state $(x_\gamma^{\rm jets}, E_T^{\rm jets})$. This correlation was calculated using the PYTHIA generator together with a detailed simulation of the detector. The procedure modifies the di-jet cross section of the PYTHIA calculation without detector effects so as to ensure that the predicted di-jet distributions as a function of $(x_\gamma^{\rm rec}, E_T^{\rm rec})$ agree with the data. Further details of the correction procedure can be found in [34]. The inner error bars reflect the statistical errors. The outer error bars shown are the statistical and systematic errors added in quadrature. The main contribution to the systematic error results from a 4% uncertainty in the knowledge of the calorimeter hadronic energy scale (Table 1). Variation of the unfolding parameters affects the measured cross section by less than 10%. The uncertainty in the determination of the trigger efficiency using redundant triggers is below 10%. The luminosity measurement is accurate to 1.5%.

The measured cross section is compared to the simulation of the PYTHIA generator (dashed curve) using the GRV-LO parton distribution functions for the photon and the proton [23, 24]. This calculation includes the leading-order QCD matrix elements together with higher-order QCD effects which are simulated by a parton shower mechanism, multiple parton interactions and hadronization. All $x_\gamma^{\rm jets}$ ranges are dominated by resolved photon processes, except for the highest region, $x_\gamma^{\rm jets} > 0.75$, where the direct photon processes give the dominant contribution. The PHOJET generator, using the same parton distribution functions and the same choice of the scale, gives results that are compatible with the PYTHIA calculation to within 20%. Also shown are two analytical calculations of the di-jet cross section in next-to-leading order QCD [30] which use the GRV-HO [23] (full curve) and GS96 [31] (dotted curve) photon parton distribution functions. In both calculations the CTEQ-4M [32] parameterization of the proton parton distribution is used. In these calculations the jet finding is based on the three final state partons. Since fragmentation effects and underlying event energy from multiple parton interactions are not included, deviations from the measured cross sections are expected. Multiple parton interactions increase the jet energy and therefore the jet cross section. The influence on the cross section has been estimated to be below 40% at small $x_\gamma^{\rm jets} \approx 0.1$ and simultaneously small $E_T^{\rm jets}$, and is negligible at $x_\gamma^{\rm jets} \approx 1$ or $E_T^{\rm jets} > 15\,\rm GeV$. The influence of the fragmentation process is maximal in the region of low $E_T^{\rm jets}$ and raises the jet cross section by at most 20% [35].

All calculations give a satisfactory description of the data overall, except for some deficiencies in the lowest $x_\gamma^{\rm jets}$ range and the two highest $x_\gamma^{\rm jets}$ ranges. In these regions, the resolved photon contribution is not well constrained from measurements of the photon structure function F_2^γ at e^+e^- colliders. The two GRV-LO and the GS96 parton distribution functions each give a good description of the F_2^γ measurements. The successful application of these parton distributions in the calculation of the di-jet cross section in ep scattering supports the universality of the photon parton distributions. However, in detail, the differences between the measurement and these calculations show that the jet data give new constraints on the parton distribution functions, especially in the region at large $x_\gamma^{\rm jets}$ and high $E_T^{\rm jets}$ which has so far not been accessible to measurements of the photon structure function F_2^γ.

6 Effective Parton Distribution of the Photon

In order to extract the parton distributions of the photon from the data, $f_{i/\gamma}$ in (4) needs to be disentangled from the sum over the different parton processes. This is not possible without further assumptions.

Here we follow the approximation procedure developed in [17]. The method is based on the leading-order matrix elements for the partonic scattering processes $qq' \to qq'$, $qg \to qg$, and $gg \to gg$ which give the dominant contribution to the total resolved photon di-jet cross section. The shapes of the angular distributions of the scattered partons are similar for all of these processes. The squared matrix elements differ in rate by the ratio of the colour factors $C_A/C_F = 9/4$. The approximation uses only one Single Effective Subprocess matrix element $M_{\rm SES}$ and combines the quark and gluon densities into new effective parton density functions

$$\tilde{f}_\gamma(x_\gamma, p_T^2) \equiv \sum_{\rm n_f} \left(f_{\rm q/\gamma}(x_\gamma, p_T^2) + f_{\bar{\rm q}/\gamma}(x_\gamma, p_T^2)\right) + \frac{9}{4}\, f_{\rm g/\gamma}(x_\gamma, p_T^2) \quad \text{and} \tag{13}$$

$$\tilde{f}_{\rm p}(x_{\rm p}, p_T^2) \equiv \sum_{\rm n_f} \left(f_{\rm q/p}(x_{\rm p}, p_T^2) + f_{\bar{\rm q}/\rm p}(x_{\rm p}, p_T^2)\right) + \frac{9}{4}\, f_{\rm g/p}(x_{\rm p}, p_T^2)\ . \tag{14}$$

The sums run over the quark flavours. The product $\tilde{f}_\gamma \tilde{f}_{\rm p} |M_{\rm SES}|^2$ then replaces the resolved photon contributions to the sum $\sum_{ij} f_{i/\gamma} f_{j/\mathrm{p}} |M_{ij}|^2$ of equation (4):

$$\frac{\mathrm{d}^4\sigma}{\mathrm{d}y\,\mathrm{d}x_\gamma\,\mathrm{d}x_\mathrm{p}\,\mathrm{d}\cos\theta^*} \approx \frac{1}{32\pi s_\mathrm{ep}} \frac{f_{\gamma/\mathrm{e}}(y)}{y} \frac{\tilde{f}_\gamma(x_\gamma, p_T^2)}{x_\gamma} \frac{\tilde{f}_\mathrm{p}(x_\mathrm{p}, p_T^2)}{x_\mathrm{p}} |M_\mathrm{SES}(\cos\theta^*)|^2 \,. \tag{15}$$

Here $\tilde{f}_\gamma(x_\gamma, p_T^2)$ can be directly determined from the measurement of the di-parton cross section. In the kinematic range which is relevant to this analysis the accuracy of the 9/4 weight in (13) was checked with a PYTHIA calculation of the di-parton cross section based on (4). The relative contributions of the quark and gluon induced di-jet events agree with this weight to better than 5% in the range $0.2 < x_\gamma < 0.7$ considered here.

6.1 Test of the Factorization of the Di-Jet Cross Section

Before the effective parton density $\tilde{f}_\gamma$ of the photon is extracted, it is shown that the factorization of the di-jet cross section (15) into effective parton densities is compatible with the measured data. If the factorization approximation is good, the shape of the parton fractional energy distribution $x_\mathrm{p}^\mathrm{rec}$ from the proton side should be independent of the parton fractional energy from the photon side x_γ^rec. In order to test this hypothesis, the four dimensions of the reconstructed di-jet distribution $N(y^\mathrm{rec}, x_\gamma^\mathrm{rec}, x_\mathrm{p}^\mathrm{rec}, \theta^{*,\mathrm{rec}})$ are reduced to two dimensions, using the two independent observables $x_\mathrm{p}^\mathrm{rec}$ and y^rec by applying the requirements $\theta^{*,\mathrm{rec}} \approx 90^\circ$ ($|\Delta\eta^\mathrm{rec}| < 1$) and $y^\mathrm{rec}\, x_\gamma^\mathrm{rec} \approx$ constant ($0.1 < y^\mathrm{rec}\, x_\gamma^\mathrm{rec} < 0.2$). The latter cut implies that the energy which enters the parton–parton scattering process from the electron side is constant. $x_\mathrm{p}^\mathrm{rec}$ is calculated from the reconstructed jet energies and pseudo-rapidities using $x_\mathrm{p}^\mathrm{rec} = \left(E_{T,1}^\mathrm{rec}\, e^{\eta_1^\mathrm{rec}} + E_{T,2}^\mathrm{rec}\, e^{\eta_2^\mathrm{rec}}\right) / (2E_\mathrm{p})$. In Fig. 3, the $x_\mathrm{p}^\mathrm{rec}$ distribution is shown in 4 different y^rec intervals. All distributions were normalized to the data sample covering the full y^rec interval, $0.2 < y^\mathrm{rec} < 0.8$. The measured ratios are compatible with having the same shape in all four y^rec bins.

Since the average parton fractional energy $\langle x_\gamma^\mathrm{rec}\rangle$ of the four $x_\mathrm{p}^\mathrm{rec}$ distributions varies between $\langle x_\gamma^\mathrm{rec}\rangle = 0.22$ and $\langle x_\gamma^\mathrm{rec}\rangle = 0.69$, the observed $x_\mathrm{p}^\mathrm{rec}$ distributions are also independent of x_γ^rec. Therefore, within the precision of the data, factorization holds in (15) and so the ansatz used to extract an effective parton distribution for the photon is meaningful.

6.2 Effects Influencing the Correction to Leading Order Parton Variables

In order to correct from the jet observables to the parton variables three effects have to be taken into account. These are multiple parton interactions, higher-order QCD effects and fragmentation effects.

In the generators used here, the fragmentation is simulated using the well tuned Lund string fragmentation model (JETSET 7.4).

Multiple parton interactions lead to an additional energy flow in the event which affects the jet rates. These effects were studied in a previous analysis using the transverse energy flow outside the jets and energy-energy correlations. These are well simulated, for example, by the PYTHIA generator [3].

Higher-order QCD effects can be studied by looking at multi-jet production. The relative contribution of events with three or more reconstructed jets above a transverse jet energy of 7 GeV amounts to 8% of the total event sample. This contribution is well described by the PYTHIA simulation.

Further results of higher-order QCD effects are an imbalance between the transverse energies of the two highest transverse energy jets and a deviation from a back-to-back configuration in the azimuth. For this study, the region of reconstructed parton fractional energies above $x_\gamma^{\rm rec} = 0.4$ is considered in order to minimize contributions of multiple parton interaction effects [3]. The missing total transverse energy in photoproduction events is small and was here required to be below $E_{T,\rm miss}^{\rm rec} = 5\,{\rm GeV}$ to ensure that the transverse jet energies were well measured.

In Fig. 4a, the shape of the transverse energy imbalance $\Delta E_T^{\rm rec} = |E_{T,1}^{\rm rec} - E_{T,2}^{\rm rec}|$ between the two jets with the highest $E_T^{\rm rec}$ is shown. Fig. 4b shows the azimuthal difference between the two jets $\Delta\phi^{\rm rec} = |\phi_1^{\rm rec} - \phi_2^{\rm rec}|$. The shape of the $\Delta E_T^{\rm rec}$ and $\Delta\phi^{\rm rec}$ distributions is described by a PYTHIA calculation which includes hard initial-state parton showers (full histogram in Fig. 4). This calculation also gives a good description of the $\Delta E_T^{\rm rec}$ and $\Delta\phi^{\rm rec}$ distributions at $x_\gamma^{\rm rec} < 0.4$ (not shown). The dashed histogram represents a calculation of the PHOJET generator in a version that does not include hard initial-state parton radiation effects: this calculation gives too small $\Delta E_T^{\rm rec}$ and too large $\Delta\phi^{\rm rec}$. We conclude that higher-order QCD effects are well modelled by parton showers.

6.3 Extraction of the Effective Parton Distribution Function

For the extraction of the effective photon parton distribution function, $\tilde{f}_\gamma$, the measured di-jet cross section was corrected to the level of the leading-order di-parton cross section using the same unfolding procedure [33] as applied in the analysis of the jet cross section described above. In this case the correlations between $(x_\gamma^{\rm jets}, E_T^{\rm jets})$ and the parton variables (x_γ, p_T) are used to correct for the fragmentation, higher-order QCD effects and underlying event energy effects. As discussed in the previous paragraph, all these effects are well modelled by the PYTHIA generator. The model dependence of the corrections was checked using the different generated event samples described in Sect. 4. Comparison of the di-parton cross section from data and a PYTHIA calculation using (4) together with the GRV-LO parton distributions and with p_T as the scale then gives the effective parton distribution of the photon in the data:

$$\tilde{f}_\gamma^{\rm DATA} = \tilde{f}_\gamma^{\rm GRV-LO} \times \frac{{\rm d}^2\sigma^{\rm DATA}/({\rm d}x_\gamma {\rm d}\log p_T^2)}{{\rm d}^2\sigma^{\rm PYTHIA,GRV-LO}/({\rm d}x_\gamma {\rm d}\log p_T^2)} \quad . \tag{16}$$

In Fig. 5 the measured effective parton distribution of the photon and its scale dependence are presented. The data are shown in two intervals of the parton fractional energy a) $0.2 < x_\gamma < 0.4$ and b) $0.4 < x_\gamma < 0.7$. The inner error bars represent the statistical errors, the outer error bars the quadratic sum of the statistical and systematic errors. In addition to the errors of the di-jet cross section, which were described in Sect. 5, the error bars include the uncertainty in the correction resulting from multiple parton scattering effects which was determined using the two event generators PYTHIA and PHOJET (Table 2).

For comparisons with the data, the effective parton distributions of the photon and the pion were calculated from the GRV-LO parameterizations [24, 36]. The pion parton distribution was scaled by the factor $\kappa \cdot 4\pi\alpha/f_\rho^2 \approx 0.9\,\alpha$ where $f_\rho^2/4\pi \approx 2.2$ represents the probability that a photon converts into a ρ meson and $\kappa \approx 2$ effectively accounts for contributions of heavier vector mesons [23]. This parton distribution therefore gives the vector meson dominance picture of the photon and is shown as the dashed curve (VDM) in Fig. 5. It differs from the measurement both in shape and absolute rate.

The GRV-LO parameterization of the photon parton distribution functions was chosen to resemble that of a hadron at small scales, $\mu \approx 0.5\,{\rm GeV}$ (not shown). At large scales $\mu \gg 1\,{\rm GeV}$, the parton densities of the photon reproduce the measurements of the photon structure function F_2^γ, which is observed to rise with $\mu^2 = Q^2$ at a rate which is compatible with the logarithmic increase that results from the pointlike term in the DGLAP QCD evolution equation (1) (see e.g. [12]).

The measurements made here show, for the first time in the context of photoproduction, the above-mentioned logarithmic dependence of photon structure on the scale, p_T, at which that structure is probed. The GRV-LO parameterization of photon structure (full curve in Fig. 5), which includes the effects of the pointlike term in the DGLAP equations, describes the measurement. If this term is excluded, as in the VDM model calculations shown here (dashed curve), it is not possible to describe the data. Further, as information on the photon quark distributions is obtained from the F_2^γ measurements, it is possible to identify the contribution they make to the effective parton distribution measured here (dotted curve). The difference between this and the measured values is a consequence of the gluon content of the photon. This is observed to contribute about 20% to the total effective parton distribution in the range $0.4 < x_\gamma < 0.7$ and about 50% in the lower x_γ range, $0.2 < x_\gamma < 0.4$.

The precision of the jet measurement is similar to that obtained in the e^+e^- experiments. The data extend the kinematic region where the parton distributions of the photon are measured to the scale $p_T^2 = 1250\,\mathrm{GeV}^2$.

7 Summary

A measurement of the double-differential inclusive di-jet cross section in terms of the parton fractional energy and the transverse energy scale was presented from H1 photoproduction data. This measurement constrains the quark and gluon distributions of the photon with a precision that is competitive with two photon data. In addition, a new kinematic range up to $x_\gamma^{\mathrm{jets}} \approx 1$ and $(E_T^{\mathrm{jets}})^2 = 2500\,\mathrm{GeV}^2$ is covered.

For the first time, an effective parton distribution of the photon was extracted from the data. The observed scale dependence shows an increase with p_T^2 that is compatible with the logarithmic increase predicted by perturbative QCD calculations of the parton content of the photon.

Acknowledgements

We are very grateful to the HERA machine group whose outstanding efforts made this experiment possible. We acknowledge the support of the DESY technical staff. We appreciate the big effort of the engineers and technicians who constructed and maintained the detector. We thank the funding agencies for financial support of this experiment. We wish to thank the DESY directorate for the support and hospitality extended to the non–DESY members of the collaboration. We wish to thank M. Drees for drawing our attention to the concept of the effective parton distribution and for discussions on the applications to the photon–proton data. We thank M. Klasen and G. Kramer for enlightening discussions on the choice of the di-jet variables and good collaboration.

References

[1] ZEUS Collab., M. Derrick et al., Phys. Lett. B322 (1994) 287.

[2] H1 Collab., T. Ahmed et al., Nucl. Phys. B445 (1995) 195.

[3] H1 Collab., S. Aid et al., Z. Phys. C70 (1996) 17.

[4] ZEUS Collab., M. Derrick et al., Phys. Lett. B384 (1996) 401.

[5] M. Erdmann, 'The Partonic Structure of the Photon', Springer Tracts in Mod. Phys. 138, Heidelberg: Springer (1997).

[6] PLUTO Collab., Ch. Berger et al., Nucl. Phys. B281 (1987) 365.

[7] JADE Collab., W. Bartel et al., Z. Phys. C24 (1984) 231.

[8] TASSO Collab., M. Althoff et al., Z. Phys. C31 (1986 527.

[9] TPC/2γ Collab., H. Aihara et al., Z. Phys. C34 (1987) 1.

[10] H. Kolanoski, 'Two Photon Physics at e^+e^- Storage Rings', Springer Tracts in Mod. Phys. 105, Heidelberg: Springer (1984)
H. Kolanoski and P. Zerwas, DESY-87-175 (1987), 'High Energy Electron-Positron Physics', Ed. A. Ali and P. Söding, Singapore, Singapore: World Scientific (1988).

[11] Ch. Berger and W. Wagner, Phys. Rep. 146 (1987) 1.

[12] AMY Collab., S.K. Sahu et al., Phys. Lett. B346 (1995) 208.

[13] TOPAZ Collab., K. Muramatsu et al. Phys. Lett. B332 (1994) 477.

[14] DELPHI Collab., P. Abreu et al., Z. Phys. C69 (1996) 223.

[15] OPAL Collab., K. Ackerstaff et al., Z. Phys. C74 (1997) 33.

[16] E. Witten, Nucl. Phys. B120 (1977) 189.

[17] B.L. Combridge and C.J. Maxwell, Nucl. Phys. B239 (1984) 429.

[18] H1 Collab., I. Abt et al., Nucl. Instr. and Methods A386 (1997) 310.
H1 Collab., I. Abt et al., Nucl. Instr. and Methods A386 (1997) 348.

[19] J. Bürger et al., Nucl. Instr. and Methods A279 (1989) 217.

[20] B. Andrieu et al., Nucl. Instr. and Methods A336 (1993) 460.

[21] J. Huth et al., Proc. of the 1990 DPF Summer Study on High Energy Physics, Snowmass, ed. E. L. Berger, World Scientific (1992) 134.

[22] T. Sjöstrand, CERN-TH-6488 (1992), Comput. Phys. Commun. 82 (1994) 74.

[23] M. Glück, E. Reya and A. Vogt, Phys. Rev. D46 (1992) 1973.

[24] M. Glück, E. Reya and A. Vogt, Z. Phys. C53 (1992) 127.

[25] T. Sjöstrand, M. Bengtsson, Comput. Phys. Commun. 43 (1987) 367.

[26] R. Engel, Z. Phys. C66 (1995) 203.

[27] R. Engel and J. Ranft, Phys. Rev. D54 (1996) 4244.

[28] A. Capella et al., Phys. Rep. 236 (1994) 225.

[29] A. Capella et al., Phys. Rev. Lett. 58 (1987) 2015.

[30] M. Klasen and G. Kramer, DESY-96-246, hep-ph@xxx.lanl.gov - 9611450 (1996).

[31] L. E. Gordon and J. K. Storrow, ANL-HEP-PR-96-33, HEP-PH-9607370 (1996).

[32] H.L. Lai et al., Phys. Rev. D51 (1995) 4763.

[33] G. D'Agostini, Nucl. Instrum. Meth. A362 (1995) 487.

[34] H. Rick, PhD thesis, Dortmund (1997), unpublished.

[35] J .M. Butterworth, L. Feld, M. Klasen, G. Kramer, Proc. of the Workshop 'Future physics at HERA', eds. G. Ingelman, A. DeRoeck, R. Klanner, Hamburg (1996) 554.

[36] M. Glück, E. Reya and A. Vogt, Z. Phys. C53 (1992) 651.

Figures

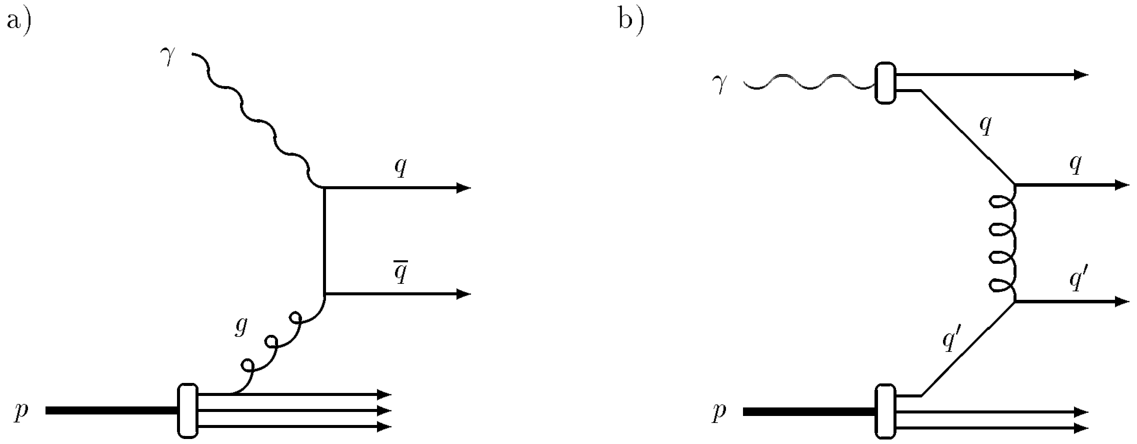

Figure 1: Diagrams for the di-jet production in γp scattering: Example for direct (a) and resolved (b) photon processes.

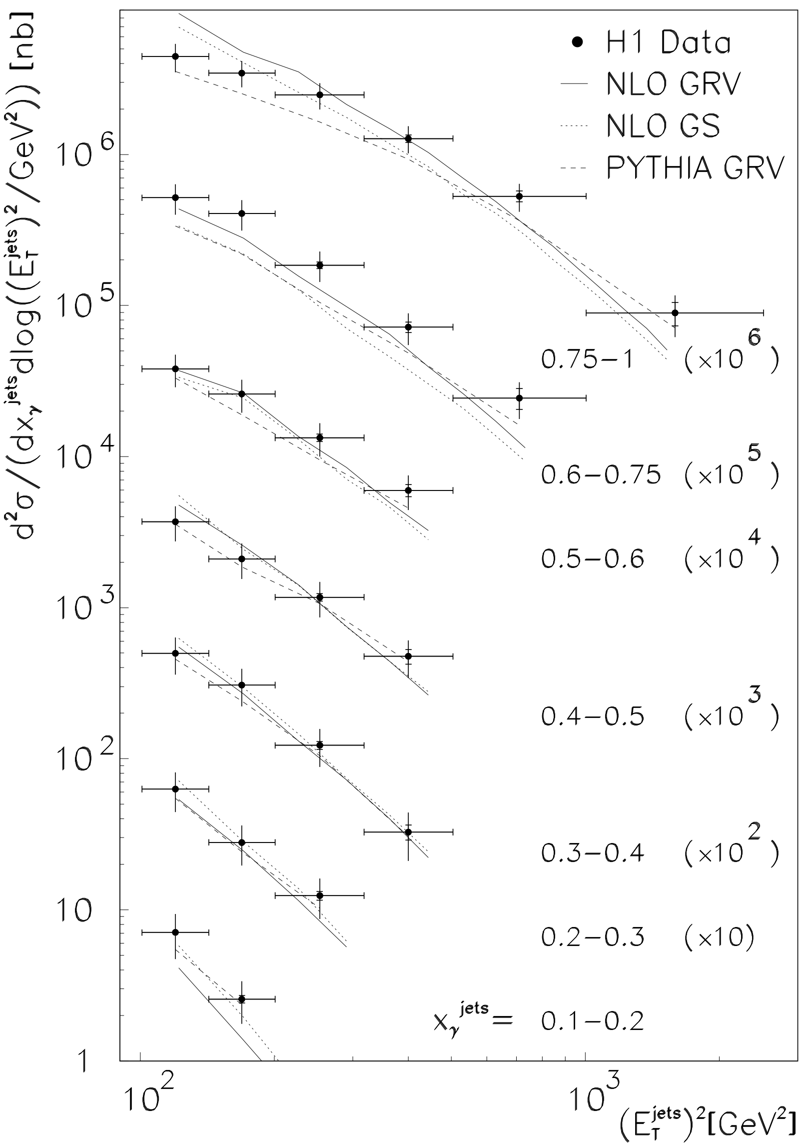

Figure 2: The measured inclusive di-jet ep cross section is shown as a function of the squared jet transverse energy $E_T^{\rm jets}$ for ranges of the reconstructed parton fractional energy $x_\gamma^{\rm jets}$ (full circles). $E_T^{\rm jets}$ is the average transverse energy of the two jets with the highest $E_T^{\rm jet}$ in the event. The average pseudo-rapidities of the jets were between $0 < (\eta^{\rm jet1} + \eta^{\rm jet2})/2 < 2$ and their difference was below $|\Delta\eta^{\rm jets}| = 1$. The transverse energies of the jets were restricted to the range $|E_T^{\rm jet1} - E_T^{\rm jet2}|/(E_T^{\rm jet1} + E_T^{\rm jet2}) < 0.25$. The cross section is integrated over the photon virtuality $Q^2 < 4\,{\rm GeV}^2$ and the relative photon energy $0.2 < y < 0.83$. The inner error bars represent the statistical errors, the outer error bars give the statistical and systematic errors, added in quadrature. The data are compared to the QCD simulation of the PYTHIA generator using the GRV-LO parton distribution functions (dashed curve) and to analytical next-to-leading (NLO) QCD calculations of the di-jet cross section [30] using the GRV-HO (full line) and GS96 (dotted line) photon parton distributions.

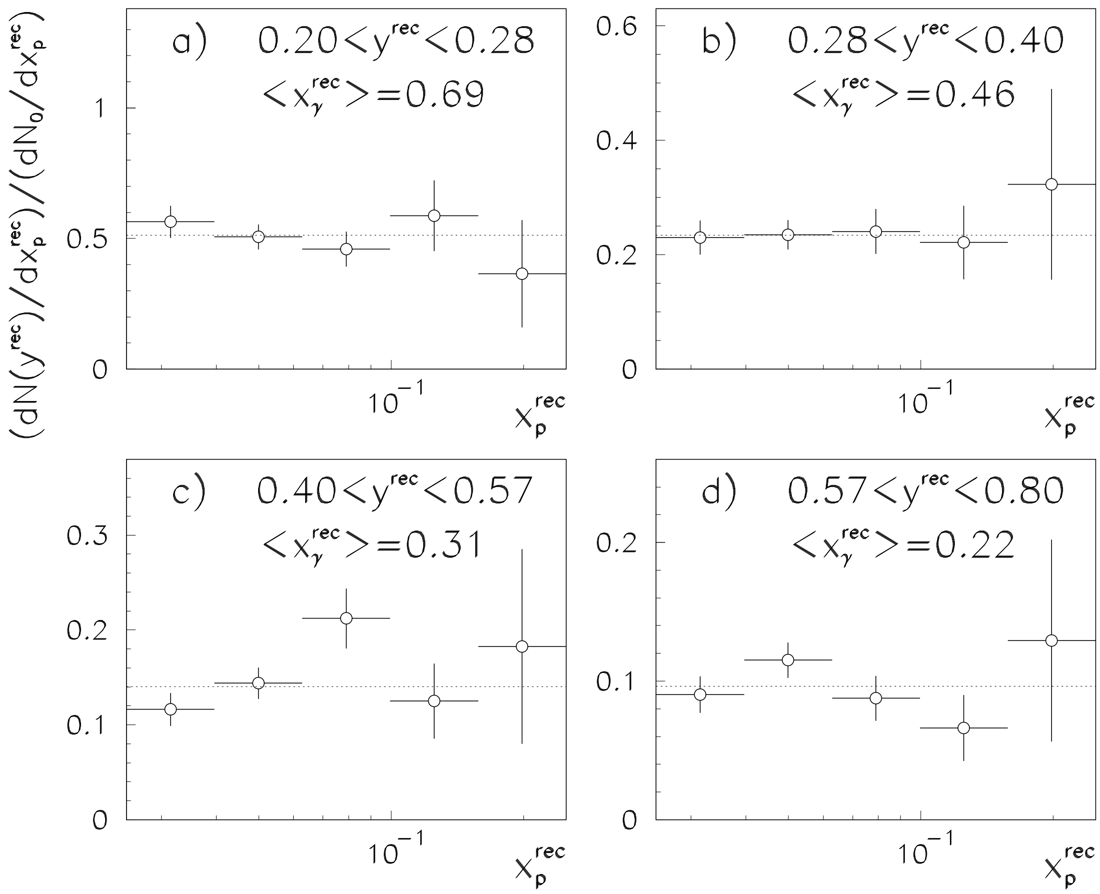

Figure 3: The distributions of the reconstructed fractional energy $x_{\mathrm{p}}^{\mathrm{rec}}$ of the parton from the proton side are shown in four bins of the photon fractional energy y^{rec}. All distributions were normalized to the $x_{\mathrm{p}}^{\mathrm{rec}}$ distribution of all events in the whole interval $0.2 < y^{\mathrm{rec}} < 0.8$, $\mathrm{d}N_0/\mathrm{d}x_{\mathrm{p}}^{\mathrm{rec}}$. Only statistical errors are shown. The dotted line represents a fit to the ratio assuming a flat distribution.

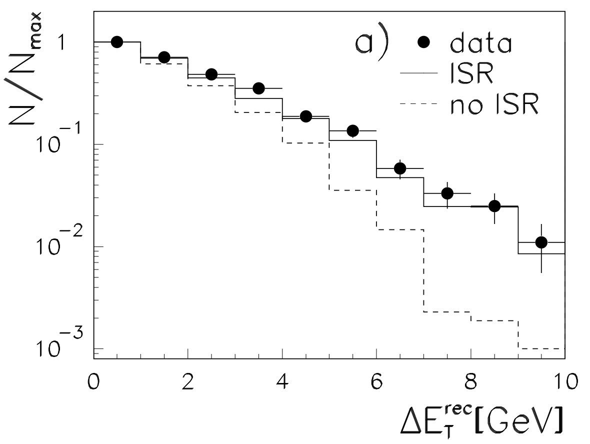

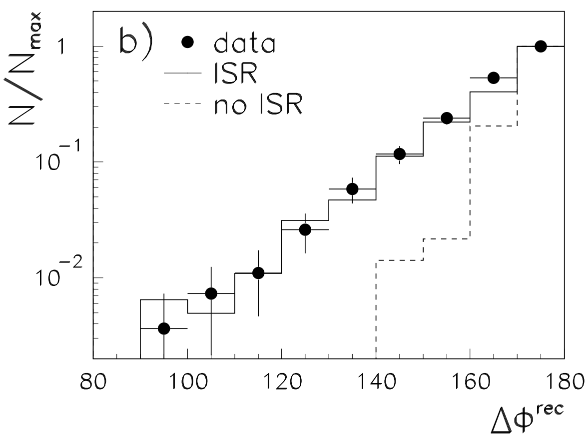

Figure 4: a) The shape of the distribution of the uncorrected jet transverse energy imbalance $\Delta E_T^{\rm rec} = |E_{T,1}^{\rm rec} - E_{T,2}^{\rm rec}|$ is shown. The distribution is normalized to the maximum number of entries $N_{\rm max}$ in a single bin. The reconstructed parton fractional energy was required to be $x_\gamma^{\rm rec} > 0.4$. The full histogram shows the prediction of the PYTHIA generator which includes hard initial-state parton radiation effects (ISR). The dashed histogram shows the calculation of the PHOJET generator in a version without hard initial-state parton radiation (no ISR). Both calculations include a detailed simulation of the detector effects. b) The shape of the uncorrected distribution of the azimuthal difference between the two jets $\Delta\phi^{\rm rec} = |\phi_1^{\rm rec} - \phi_2^{\rm rec}|$ is shown. The histogram assignments are as in a).

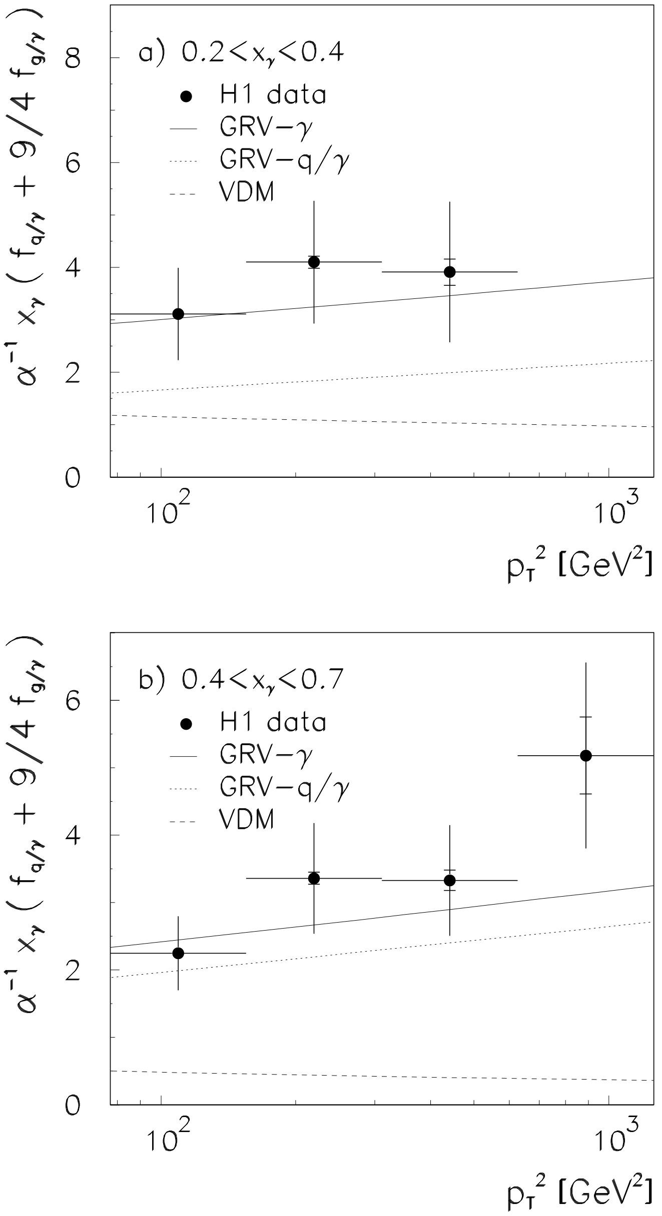

Figure 5: The leading order effective parton distribution of the photon $x_\gamma \tilde{f}_\gamma(x_\gamma, p_T^2) = x_\gamma(f_{\mathrm{q}/\gamma}(x_\gamma, p_T^2) + 9/4\, f_{\mathrm{g}/\gamma}(x_\gamma, p_T^2))$ is shown as a function of the squared parton transverse momentum p_T^2. The $f_{\mathrm{q}/\gamma}$ represents here the sum over all quarks and anti-quarks and $f_{\mathrm{g}/\gamma}$ is the gluon density. The distribution was divided by the fine structure constant α and averaged over parton fractional energies in the ranges a) $0.2 < x_\gamma < 0.4$ and b) $0.4 < x_\gamma < 0.7$. The inner error bars represent the statistical errors, the outer error bars give the statistical and systematic errors, added in quadrature. The data are compared to the effective parton distribution of the photon which includes the pointlike coupling of the photon to quarks (full curve) and to a vector meson dominance (VDM) ansatz for the photon (dashed curve). The dotted curve shows the quark part of the effective parton distribution. All three curves were calculated using the GRV-LO parton distribution functions.

Tables

$x_\gamma^{\rm jets}$ min	$x_\gamma^{\rm jets}$ max	$\log(E_T^{\rm jets}/\mathrm{GeV})^2$ min	$\log(E_T^{\rm jets}/\mathrm{GeV})^2$ max	cross section $\frac{d^2\sigma^{ep\to 2\rm jets}}{dx_\gamma^{\rm jets} d\log((E_T^{\rm jets})^2/\mathrm{GeV}^2)}$ [nb]	error stat.	error syst. E-scale	error syst. other	error total
0.10	0.20	2.00	2.15	7.42	±0.27	±2.00	±0.83	±2.19
		2.15	2.30	2.62	±0.14	±0.71	±0.29	±0.78
0.20	0.30	2.00	2.15	6.31	±0.20	±1.58	±0.71	±1.74
		2.15	2.30	2.83	±0.13	±0.71	±0.32	±0.79
		2.30	2.50	1.23	±0.08	±0.31	±0.14	±0.35
0.30	0.40	2.00	2.15	5.06	±0.19	±1.16	±0.57	±1.31
		2.15	2.30	3.00	±0.14	±0.69	±0.34	±0.78
		2.30	2.50	1.27	±0.08	±0.29	±0.14	±0.33
		2.50	2.70	0.30	±0.03	±0.09	±0.03	±0.10
0.40	0.50	2.00	2.15	3.81	±0.15	±0.80	±0.43	±0.92
		2.15	2.30	2.19	±0.10	±0.46	±0.24	±0.53
		2.30	2.50	1.16	±0.07	±0.24	±0.13	±0.28
		2.50	2.70	0.46	±0.05	±0.10	±0.05	±0.12
0.50	0.60	2.00	2.15	4.05	±0.16	±0.77	±0.45	±0.91
		2.15	2.30	2.71	±0.13	±0.51	±0.30	±0.61
		2.30	2.50	1.27	±0.08	±0.24	±0.14	±0.29
		2.50	2.70	0.60	±0.05	±0.11	±0.07	±0.14
0.60	0.75	2.00	2.15	5.11	±0.18	±0.84	±0.61	±1.06
		2.15	2.30	4.15	±0.16	±0.69	±0.46	±0.84
		2.30	2.50	2.00	±0.10	±0.33	±0.22	±0.41
		2.50	2.70	0.75	±0.06	±0.12	±0.08	±0.16
		2.70	3.00	0.27	±0.04	±0.04	±0.03	±0.07
0.75	1.00	2.00	2.15	4.32	±0.18	±0.54	±0.59	±0.82
		2.15	2.30	3.43	±0.14	±0.42	±0.38	±0.59
		2.30	2.50	2.50	±0.11	±0.31	±0.28	±0.43
		2.50	2.70	1.25	±0.07	±0.16	±0.14	±0.22
		2.70	3.00	0.54	±0.04	±0.07	±0.06	±0.10
		3.00	3.40	0.09	±0.02	±0.02	±0.01	±0.03

Table 1: Inclusive double-differential di-jet cross section in bins of $x_\gamma^{\rm jets}$ and $\log(E_T^{\rm jets}/\mathrm{GeV})^2$. The limits of the bins are listed in the first four columns. For each bin a cross section number is given together with the statistical and systematic uncertainties. The error induced by the 4% uncertainty of the hadronic calibration of the calorimeter (E-scale) is listed separately.

x_γ	$p_T^2[\mathrm{GeV}^2]$	$\frac{1}{\alpha}x_\gamma \tilde{f}_\gamma(x_\gamma, p_T^2)$	σ_{stat}	σ_{syst} exp.	σ_{syst} model dep.	σ_{total}
0.3	112	3.11	$\pm$ 0.07	$\pm$ 0.82	$\pm$ 0.31	$\pm$ 0.88
	224	4.10	$\pm$ 0.11	$\pm$ 1.09	$\pm$ 0.41	$\pm$ 1.17
	447	3.91	$\pm$ 0.25	$\pm$ 1.25	$\pm$ 0.48	$\pm$ 1.34
0.55	112	2.25	$\pm$ 0.05	$\pm$ 0.50	$\pm$ 0.23	$\pm$ 0.55
	224	3.36	$\pm$ 0.09	$\pm$ 0.74	$\pm$ 0.34	$\pm$ 0.82
	447	3.33	$\pm$ 0.15	$\pm$ 0.73	$\pm$ 0.37	$\pm$ 0.82
	891	5.18	$\pm$ 0.57	$\pm$ 1.14	$\pm$ 0.78	$\pm$ 1.38

Table 2: The effective photon parton distribution $x_\gamma \tilde{f}_\gamma$ is shown as a function of the parton fractional energy x_γ and the transverse momentum p_T^2 of the scattered partons. The systematic errors are separated into contributions from experimental uncertainties and model dependencies. The total error (σ_{total}) corresponds to the quadratic sum of the statistical (σ_{stat}) and systematic (σ_{syst}) errors.